



# Locking-free stabilized conforming nodal integration for meshfree Mindlin–Reissner plate formulation

Dongdong Wang, Jiun-Shyan Chen \*

*Department of Civil & Environmental Engineering, University of California – Los Angeles, 5731G Boelter Hall,  
Los Angeles, CA 90095-1593, USA*

Received 6 April 2003; received in revised form 2 September 2003; accepted 4 December 2003

## Abstract

The cause of shear locking in Mindlin–Reissner plate formulation is due to the inability of the numerical formulation in representing pure bending mode without producing parasitic shear deformation (lack of Kirchhoff mode). To resolve shear locking in meshfree formulation of Mindlin–Reissner plates, the following two issues are addressed: (1) construction of approximation functions capable of reproducing Kirchhoff modes, and (2) formulation of domain integration of Galerkin weak form capable of producing exact solution under pure bending condition. In this study, we first identify the Kirchhoff mode reproducing conditions (KMRC), and show that the employment of a second order monomial basis in the reproducing kernel or moving least-square approximation of translational and rotational degrees of freedom is an effective means to meet KMRC. Next, the integration constraints that fulfill bending exactness (BE) in the Galerkin meshfree discretization of Mindlin–Reissner plate are derived. A nodal integration with curvature smoothing stabilization that fulfills BE is then formulated for Mindlin–Reissner plate. The curvature smoothing stabilization is introduced in the nodally integrated Galerkin weak form. The resulting meshfree formulation is stable and free of shear locking in the limit of thin plate. Both computational efficiency and accuracy are achieved in the proposed meshfree Mindlin–Reissner plate formulation.

© 2004 Elsevier B.V. All rights reserved.

*Keywords:* Meshfree method; Kirchhoff mode reproducing conditions; Curvature smoothing; Bending exactness; Shear locking

## 1. Introduction

Meshfree methods developed in recent years allow sufficient flexibility in customizing the approximation functions for desired smoothness, accuracy, or special characteristics of particular engineering and scientific problems. The Kirchhoff plate problem is one typical example where the  $C^1$  continuity can be easily achieved using moving least-squares approximation [15,16]. Despite of these attractive features, several authors have reported locking difficulties in constrained problems using standard meshfree methods. For

\* Corresponding author.

*E-mail address:* [jschen@seas.ucla.edu](mailto:jschen@seas.ucla.edu) (J.-S. Chen).

example, the constraint ratios in the reproducing kernel approximation with linear basis are far from optimum for incompressible problems [5]. The study of the fundamental modes and their corresponding energy further identified that the locking can never be completely suppressed simply by increasing the support size of approximation function [11]. A pressure projection method [4,5] and selective reduced integration method [8] have been proposed to resolve incompressible locking. In Mindlin–Reissner plate, employing approximation function for rotational degrees of freedom as the derivatives of the approximation function for translational degrees of freedom has also been introduced to resolve shear locking [9,14]. In [10], higher order basis functions have been employed in h-p cloud method to relieve the shear locking.

Locking can also be relieved by using a nodal integration or collocation techniques, but they often are suffered by the rank deficiency and thus produce kinematic modes [1]. A stabilized conforming nodal integration (SCNI) has been proposed as a stabilization mechanism for nodal integration [6,7] of meshfree Galerkin weak form. In this approach, the strain smoothing stabilization has been introduced in SCNI to meet integration constraints and thus fulfills the linear exactness in the Galerkin approximation of the second order partial differential equations. This approach also significantly reduces computation time due to the nature of nodal integration.

The cause of shear locking in Mindlin–Reissner plate formulation is due to (1) inability in the approximation functions to reproduce Kirchhoff mode, and (2) the incapability of the numerical method to achieve pure bending exactness (BE) in the Galerkin approximation. The first condition is related to the approximation of kinematic variables, and the second condition is associated with both the approximation of kinematic variables and the integration of weak form. In this study, the reproducibility of Kirchhoff mode, termed Kirchhoff mode reproducing conditions (KMRC), is first analyzed for Mindlin–Reissner plate. The approximation functions of displacement and rotations are constructed to meet KMRC. The conditions for vanishing parasitic shear deformation under pure bending are obtained. Next, the integration constraints for achieving BE are derived, and a curvature smoothing is proposed to meet bending integration constraints and to provide stability to the nodally integrated weak form.

This paper is organized as follows. The basic equations of Mindlin–Reissner plate and meshfree approximation are reviewed in Section 2. The KMRC and bending integration constraints for BE in Mindlin–Reissner plate theory are derived, and reproducing kernel shape functions that meet KMRC are presented in Section 3. In Section 4, a curvature smoothing stabilization and the corresponding discrete meshfree equation formulated via an assumed strain method to fulfill BE are introduced. Some numerical examples are presented in Section 5. Concluding remarks are drawn in Section 6.

## 2. Basic equations

### 2.1. Kinematics of Mindlin–Reissner plate

Consider a plate occupying a domain  $\mathcal{B} = \Omega \times (-t/2, t/2)$ , where  $\Omega \subset \mathbb{R}^2$  represents the mid-plane of the plate with boundary  $\Gamma$  and  $t$  is the plate thickness. In Mindlin–Reissner plate theory, the in-plane displacements  $u$  and  $v$  are assumed to vary linearly with section rotations  $\theta_1$  and  $\theta_2$  through the plate thickness  $t$ . In addition, the normal stress  $\sigma_{33}$  is assumed to be zero. The sign conventions adopted in this paper are shown in Fig. 1.

The displacement field can be expressed as

$$\begin{pmatrix} u_1 \\ u_2 \\ u_3 \end{pmatrix} = \begin{pmatrix} u \\ v \\ w \end{pmatrix} = \begin{pmatrix} -z\theta_1(x, y) \\ -z\theta_2(x, y) \\ w(x, y) \end{pmatrix}. \quad (2.1)$$

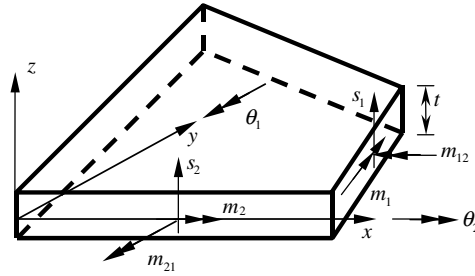


Fig. 1. Sign conventions for Mindlin–Reissner plate.

Accordingly, curvature and shear strain are presented as follows:

$$\epsilon_{\alpha\beta}^b = -z\kappa_{\alpha\beta}, \tag{2.2}$$

$$\kappa_{\alpha\beta} = \frac{1}{2}(\theta_{\alpha,\beta} + \theta_{\beta,\alpha}), \tag{2.3}$$

$$\gamma_\beta = w_{,\beta} - \theta_\beta, \tag{2.4}$$

where the subscripts  $\alpha$  and  $\beta$  range from 1 to 2.

The weak form of Mindlin–Reissner plate is stated as follows:

$$\int_{\Omega} \delta\kappa_{\alpha\beta} D_{\alpha\beta\eta\xi}^b \kappa_{\eta\xi} d\Omega + \int_{\Omega} \delta\gamma_\alpha D_{\alpha\beta}^s \gamma_\beta d\Omega + \int_{\Gamma^h} \delta\theta_\alpha \bar{m}_\alpha d\Gamma - \int_{\Omega} \delta w q d\Omega = 0, \tag{2.5}$$

$$u_i = \bar{u}_i \quad \text{on } \Gamma^g, \tag{2.6}$$

where  $\alpha$  and  $\beta$  range from 1 to 2,  $i$  ranges from 1 to 3,  $q$  is the applied transverse loading per unit area,  $\bar{m}_\alpha$  and  $\bar{u}_i$  are the prescribed boundary moments and deflection or rotation on  $\Gamma^h$  and  $\Gamma^g$ , respectively, and  $D_{\alpha\beta\eta\xi}^b$  and  $D_{\alpha\beta}^s$  are bending and shear elasticity tensors, respectively:

$$D_{\alpha\beta\eta\xi}^b = \frac{h^3}{12} [\bar{\lambda} \delta_{\alpha\beta} \delta_{\eta\xi} + \mu (\delta_{\alpha\eta} \delta_{\beta\xi} + \delta_{\alpha\xi} \delta_{\beta\eta})], \quad \bar{\lambda} = \frac{vE}{1-v^2}, \tag{2.7}$$

$$D_{\alpha\beta}^s = kt\mu\delta_{\alpha\beta}. \tag{2.8}$$

In the above equation,  $E$ ,  $v$  and  $\mu$  are Young’s modulus, Poisson’s ratio, and shear modulus respectively, and  $k = 5/6$  is the shear correction factor.

For convenience, the corresponding matrix form of Eq. (2.5) is written as

$$\int_{\Omega} \delta\boldsymbol{\kappa}^T \mathbf{D}^b \boldsymbol{\kappa} d\Omega + \int_{\Omega} \delta\boldsymbol{\gamma}^T \mathbf{D}^s \boldsymbol{\gamma} d\Omega + \int_{\Gamma^h} \delta\boldsymbol{\theta}^T \bar{\mathbf{m}} d\Gamma - \int_{\Omega} \delta w q d\Omega = 0. \tag{2.9}$$

The matrices are defined as follows:

$$\mathbf{D}^b = \frac{Et^3}{12(1-v^2)} \begin{pmatrix} 1 & v & 0 \\ v & 1 & 0 \\ 0 & 0 & (1-v)/2 \end{pmatrix}, \tag{2.10}$$

$$\mathbf{D}^s = tk\mu \begin{pmatrix} 1 & 0 \\ 0 & 1 \end{pmatrix}, \tag{2.11}$$

$$\boldsymbol{\kappa} = \begin{pmatrix} \kappa_{11} \\ \kappa_{22} \\ 2\kappa_{12} \end{pmatrix} = \begin{pmatrix} \frac{\partial \theta_1}{\partial x_1} \\ \frac{\partial \theta_2}{\partial x_2} \\ \frac{\partial \theta_1}{\partial x_2} + \frac{\partial \theta_2}{\partial x_1} \end{pmatrix}, \quad (2.12)$$

$$\boldsymbol{\gamma} = \begin{pmatrix} \gamma_1 \\ \gamma_2 \end{pmatrix} = \begin{pmatrix} w_{,1} - \theta_1 \\ w_{,2} - \theta_2 \end{pmatrix}, \quad (2.13)$$

$$\boldsymbol{\theta} = \begin{pmatrix} \theta_1 \\ \theta_2 \end{pmatrix}. \quad (2.14)$$

The moment vector  $\mathbf{m}$  is related to curvature  $\boldsymbol{\kappa}$  via

$$\mathbf{m} = \begin{pmatrix} m_1 \\ m_2 \\ m_{12} \end{pmatrix} = -\mathbf{D}^b \boldsymbol{\kappa}. \quad (2.15)$$

## 2.2. MLS/RK approximation

To construct the meshfree approximation of kinematic variables in the Mindlin–Reissner plate, the moving-least squares (MLS) [18] (used in Element Free Galerkin [2,3]) and reproducing kernel (RK) approximation [19–21] are reviewed in this sub-section. Consider a domain  $\Omega$  which is discretized by a set of nodes  $\mathbf{x}_I$ ,  $I = 1, \dots, \text{NP}$ , the MLS or RK approximation of a variable  $u(\mathbf{x})$ , denoted by  $u^h(\mathbf{x})$ , can be expressed as

$$u^h(\mathbf{x}) = \sum_{I=1}^{\text{NP}} \Psi_I(\mathbf{x}) d_I, \quad (2.16)$$

where

$$\Psi_I(\mathbf{x}) = \mathbf{H}^T(\mathbf{x} - \mathbf{x}_I) \mathbf{b}(\mathbf{x}) \phi_{a_I}(\mathbf{x} - \mathbf{x}_I). \quad (2.17)$$

Here  $\Psi_I$  and  $d_I$  are the shape function and nodal parameter associated with node  $I$ , respectively,  $\phi_{a_I}(\mathbf{x} - \mathbf{x}_I)$  is the kernel function which centers at  $\mathbf{x}_I$  and has a compact support  $a_I$ , and  $\mathbf{H}^T(\mathbf{x} - \mathbf{x}_I)$  is a vector of  $n$ th order monomial basis

$$\mathbf{H}^T(\mathbf{x} - \mathbf{x}_I) = [1 \quad x_1 - x_{I1} \quad x_2 - x_{I2} \quad \cdots \quad (x_1 - x_{I1})^n \quad \cdots \quad (x_2 - x_{I2})^n]. \quad (2.18)$$

The coefficient vector  $\mathbf{b}^T(\mathbf{x}) = [b_{00}(\mathbf{x}) \quad b_{10}(\mathbf{x}) \quad b_{01}(\mathbf{x}) \quad \cdots \quad b_{n0}(\mathbf{x}) \quad \cdots \quad b_{0n}(\mathbf{x})]$  is obtained by imposing the following  $n$ th order reproducing conditions:

$$\sum_{I=1}^{\text{NP}} \Psi_I(\mathbf{x}) x_{I1}^i x_{I1}^j = x_1^i x_2^j, \quad 0 \leq i + j \leq n. \quad (2.19)$$

Equivalently,

$$\sum_{I=1}^{\text{NP}} \Psi_I(\mathbf{x}) (x_1 - x_{I1})^i (x_2 - x_{I2})^j = \delta_{i0} \delta_{j0}, \quad 0 \leq i + j \leq n, \quad (2.20)$$

or

$$\sum_{I=1}^{\text{NP}} \Psi_I(\mathbf{x}) \mathbf{H}(\mathbf{x} - \mathbf{x}_I) = \mathbf{H}(\mathbf{0}). \quad (2.21)$$

Obtaining  $\mathbf{b}(\mathbf{x})$  from Eq. (2.21) yields the following MSL/RK shape function:

$$\Psi_I(\mathbf{x}) = \mathbf{H}^T(\mathbf{0})\mathbf{M}^{-1}(\mathbf{x})\mathbf{H}(\mathbf{x} - \mathbf{x}_I)\phi_{a_I}(\mathbf{x} - \mathbf{x}_I), \tag{2.22}$$

where

$$\mathbf{M}(\mathbf{x}) = \sum_{I=1}^{NP} \mathbf{H}(\mathbf{x} - \mathbf{x}_I)\mathbf{H}^T(\mathbf{x} - \mathbf{x}_I)\phi_{a_I}(\mathbf{x} - \mathbf{x}_I). \tag{2.23}$$

From the reproducing conditions (2.19), it can be easily shown the following properties:

$$\sum_{I=1}^{NP} \frac{\partial^{r+s}[\Psi_I(\mathbf{x})]}{\partial x_1^r \partial x_2^s} x_1^i x_2^j = \frac{i!j!}{(i-r)!(j-s)!} x_1^{i-r} x_2^{j-s}, \quad 0 \leq (i+j), (r+s) \leq n. \tag{2.24}$$

### 3. Integration constraints for plate bending

In this section, we first construct shape functions that can reproduce Kirchhoff modes in shear deformable plates under pure bending. The bending integration constraints are then derived to achieve bending exactness in the Galerkin meshfree formulation of Mindlin–Reissner plate.

#### 3.1. Kirchhoff mode reproducing conditions

Let the transverse deflection and rotations be approximated by MLS/RK shape functions as

$$\mathbf{u}^h = \begin{pmatrix} w^h \\ \theta_1^h \\ \theta_2^h \end{pmatrix} = \sum_{I=1}^{NP} \Psi_I \begin{pmatrix} w_I \\ \theta_{1I} \\ \theta_{2I} \end{pmatrix} = \sum_{I=1}^{NP} \Psi_I(\mathbf{x}) \mathbf{d}_I. \tag{3.1}$$

The corresponding approximation of shear strain  $\boldsymbol{\gamma}$  and curvature  $\boldsymbol{\kappa}$  are

$$\boldsymbol{\gamma}^h = \begin{pmatrix} \gamma_1^h \\ \gamma_2^h \end{pmatrix} = \sum_{I=1}^{NP} \begin{pmatrix} \Psi_{I,1} w_I - \Psi_I \theta_{1I} \\ \Psi_{I,2} w_I - \Psi_I \theta_{2I} \end{pmatrix} = \sum_{I=1}^{NP} \mathbf{B}_I^s \mathbf{d}_I, \tag{3.2}$$

$$\boldsymbol{\kappa}^h = \begin{pmatrix} \kappa_{11}^h \\ \kappa_{22}^h \\ 2\kappa_{12}^h \end{pmatrix} = \begin{pmatrix} \frac{\partial \theta_1^h}{\partial x_1} \\ \frac{\partial \theta_2^h}{\partial x_2} \\ \frac{\partial \theta_1^h}{\partial x_2} + \frac{\partial \theta_2^h}{\partial x_1} \end{pmatrix} = \sum_{I=1}^{NP} \begin{pmatrix} \Psi_{I,1} \theta_{1I} \\ \Psi_{I,2} \theta_{2I} \\ \Psi_{I,2} \theta_{1I} + \Psi_{I,1} \theta_{2I} \end{pmatrix} = \sum_{I=1}^{NP} \mathbf{B}_I^b \mathbf{d}_I, \tag{3.3}$$

$$\mathbf{B}_I^b = \begin{pmatrix} 0 & \Psi_{I,x} & 0 \\ 0 & 0 & \Psi_{I,y} \\ 0 & \Psi_{I,y} & \Psi_{I,x} \end{pmatrix}, \tag{3.4}$$

$$\mathbf{B}_I^s = \begin{pmatrix} \Psi_{I,x} & -\Psi_I & 0 \\ \Psi_{I,y} & 0 & -\Psi_I \end{pmatrix}, \tag{3.5}$$

$$\mathbf{d}_I = \begin{pmatrix} w_I \\ \theta_{1I} \\ \theta_{2I} \end{pmatrix}. \tag{3.6}$$

We define the Kirchhoff mode reproducing conditions (KMRC) as follows:

Let  $\mathbf{d}_I^b$  be the nodal-valued vector of a pure bending deformation, then the following conditions should be satisfied:

$$\sum_{I=1}^{NP} \mathbf{B}_I^s \mathbf{d}_I^b = \mathbf{0}, \tag{3.7}$$

$$\sum_{I=1}^{NP} \mathbf{B}_I^b \mathbf{d}_I^b = \text{const.} \tag{3.8}$$

Let  $\mathbf{d}_I^b$  be the nodal-valued vector of a pure bending deformation:

$$\mathbf{d}_I^b = \begin{pmatrix} \sum_{p+q=0}^2 c_{pq} x_{1I}^p x_{2I}^q \\ \sum_{p+q=1}^2 c_{pq} p x_{1I}^{p-1} x_{2I}^q \\ \sum_{p+q=1}^2 c_{pq} q x_{1I}^p x_{2I}^{q-1} \end{pmatrix}. \tag{3.9}$$

Substituting Eq. (3.9) into Eqs. (3.7) and (3.8) leads to the following requirements for KMRC:

$$\sum_{I=1}^{NP} \Psi_{I,1} \left( \sum_{p+q=0}^2 c_{pq} x_{1I}^p x_{2I}^q \right) - \sum_{I=1}^{NP} \Psi_I \left( \sum_{p+q=1}^2 c_{pq} p x_{1I}^{p-1} x_{2I}^q \right) = 0, \tag{3.10a}$$

$$\sum_{I=1}^{NP} \Psi_{I,2} \left( \sum_{p+q=0}^2 c_{pq} x_{1I}^p x_{2I}^q \right) - \sum_{I=1}^{NP} \Psi_I \left( \sum_{p+q=1}^2 c_{pq} q x_{1I}^p x_{2I}^{q-1} \right) = 0, \tag{3.10b}$$

$$\sum_{I=1}^{NP} \Psi_{I,1} \left( \sum_{p+q=1}^2 c_{pq} p x_{1I}^{p-1} x_{2I}^q \right) = \text{const}, \tag{3.10c}$$

$$\sum_{I=1}^{NP} \Psi_{I,2} \left( \sum_{p+q=1}^2 c_{pq} q x_{1I}^p x_{2I}^{q-1} \right) = \text{const}, \tag{3.10d}$$

$$\sum_{I=1}^{NP} \left( \Psi_{I,1} \left( \sum_{p+q=1}^2 c_{pq} q x_{1I}^p x_{2I}^{q-1} \right) + \Psi_{I,2} \left( \sum_{p+q=1}^2 c_{pq} p x_{1I}^{p-1} x_{2I}^q \right) \right) = \text{const}. \tag{3.10e}$$

Eqs. (3.10a) and (3.10b) can be reduced to

$$\sum_{I=1}^{NP} \Psi_{I,i} = 0, \tag{3.11a}$$

$$\sum_{I=1}^{NP} \Psi_{I,i} x_{1I}^p x_{2I}^q - \sum_{I=1}^{NP} \Psi_I [(x_1^p x_2^q)_{,i}]_I = 0 \quad \text{for } p + q = 1, 2. \tag{3.11b}$$

It can be easily shown that for meeting Eqs. (3.11a) and (3.11b), the shape functions have to hold the following properties:

$$\sum_{I=1}^{NP} \Psi_I x_{1I}^p x_{2I}^q = x_1^p x_2^q \quad \text{for } p + q = 0, 1, 2, \tag{3.12}$$

and it follows that

$$\sum_{I=1}^{NP} \Psi_{I,i} x_1^p x_2^q = (x_1^p x_2^q)_{,i} \quad \text{and} \quad \sum_{I=1}^{NP} \Psi_I [(x_1^p x_2^q)_{,i}]_I = (x_1^p x_2^q)_{,i} \quad \text{for } p + q = 0, 1, 2. \quad (3.13)$$

An straightforward extension of Eq. (3.13) is

$$\sum_{I=1}^{NP} \Psi_{I,i} [(x_1^p x_2^q)_{,j}]_I = (x_1^p x_2^q)_{,ij} = \text{const.} \quad \text{for } p + q = 0, 1, 2 \quad (3.14)$$

and this satisfies the conditions in Eqs. (3.10c)–(3.10e).

It is thus concluded that KMRC holds if the MLS/RK shape functions meet Eq. (3.12), and this can be achieved by employing quadratic basis in the MLS/RK shape functions in Eq. (2.22):

$$\mathbf{H}^T(\mathbf{x}) = [1 \quad x_1 \quad x_2 \quad x_1^2 \quad x_1 x_2 \quad x_2^2]. \quad (3.15)$$

### 3.2. Integration constraints

In this section, we identify the criteria for Galerkin method to fulfill bending exactness (BE) in the Mindlin–Reissner plate. The requirements for yielding an exact solution in the Galerkin meshfree discretization of Mindlin–Reissner plate formulation under pure bending condition can be realized by enforcing a pure bending deformation to satisfy the discrete equilibrium equation corresponding to the weak form of the Mindlin–Reissner problem subjected to essential and natural boundary conditions that are consistent with the pure bending deformation.

Introducing a pure bending vector  $\mathbf{d}^b$  of Eq. (3.9) into weak form of Eq. (3.2), it can be seen immediately that the shear strain vector  $\boldsymbol{\gamma}^h = \sum_{I=1}^{NP} \mathbf{B}_I^s \mathbf{d}_I^b = \mathbf{0}$  if shape functions meet KMRC for a pure bending vector  $\mathbf{d}^b$  of Eq. (3.9). Further taking shear force  $q = 0$  for pure bending we have the following reduced weak form for pure bending:

$$\int_{\Omega} \delta \boldsymbol{\kappa}^{hT} \mathbf{D}^b \boldsymbol{\kappa}^h \, d\Omega = - \int_{\Gamma^h} \delta \boldsymbol{\theta}^{hT} \bar{\mathbf{m}}^b \, d\Gamma. \quad (3.16)$$

The discrete form of the above equation is

$$\mathbf{f}_I^{\text{int}} = \mathbf{f}_I^{\text{ext}}, \quad (3.17)$$

$$\mathbf{f}_I^{\text{int}} = \int_{\Omega} (\mathbf{B}_I^b)^T \mathbf{D}^b \mathbf{B}^b \mathbf{d}^b \, d\Omega, \quad (3.18)$$

$$\mathbf{f}_I^{\text{ext}} = - \int_{\Gamma^h} \mathbf{N}_I^T \bar{\mathbf{m}}^b \, d\Gamma, \quad (3.19)$$

where

$$\mathbf{N}_I^T = \begin{pmatrix} 0 & 0 & 0 \\ 0 & \Psi_I & 0 \\ 0 & 0 & \Psi_I \end{pmatrix} \quad (3.20)$$

and  $\bar{\mathbf{m}}^b$  is the applied boundary bending moment vector consistent with a pure bending deformation.

Satisfaction of KMRC yields a constant curvature vector  $\mathbf{B}^b \mathbf{d}^b = \boldsymbol{\kappa}^b$  and thus a constant moment vector  $\mathbf{m}^b = -\mathbf{D}^b \boldsymbol{\kappa}^b$ . Hence the internal force in Eq. (3.18) corresponding to a pure bending deformation reads

$$\mathbf{f}_I^{\text{int}} = - \int_{\Omega} (\mathbf{B}_I^b)^T \mathbf{m}^b \, d\Omega = - \int_{\Omega} (\mathbf{B}_I^b)^T \, d\Omega \mathbf{m}^b. \quad (3.21)$$

Further, the kinematically consistent applied moment corresponding to the pure bending deformation is

$$\bar{\mathbf{m}}^b = \begin{pmatrix} \bar{m}_1^b \\ \bar{m}_2^b \end{pmatrix} = \begin{pmatrix} n_1 & 0 & n_2 \\ 0 & n_2 & n_1 \end{pmatrix} \mathbf{m}^b \quad (3.22)$$

and thus the associated external force of Eq. (3.19) can be rewritten as

$$\mathbf{f}_I^{\text{ext}} = - \int_{\Gamma^h} \mathbf{E}_I^T \, d\Gamma \mathbf{m}^b, \quad (3.23)$$

where

$$\mathbf{E}_I^T = \begin{pmatrix} 0 & 0 & 0 \\ \Psi_I n_1 & 0 & \Psi_I n_2 \\ 0 & \Psi_I n_2 & \Psi_I n_1 \end{pmatrix}. \quad (3.24)$$

For discrete equilibrium  $\mathbf{f}_I^{\text{int}} = \mathbf{f}_I^{\text{ext}}$ , we have

$$\int_{\Omega} (\mathbf{B}_I^b)^T \, d\Omega \mathbf{m}^b = \int_{\Gamma^h} \mathbf{E}_I^T \, d\Gamma \mathbf{m}^b. \quad (3.25)$$

Since  $\mathbf{m}^b = -\mathbf{D}^b \boldsymbol{\kappa}^b$  is a constant vector with arbitrary coefficients  $c_{20}$ ,  $c_{11}$ ,  $c_{02}$  in  $\boldsymbol{\kappa}^b$  of Eq. (3.9), Eq. (3.25) yields

$$\int_{\Omega} (\mathbf{B}_I^b)^T \, d\Omega = \int_{\Gamma^h} \mathbf{E}_I^T \, d\Gamma. \quad (3.26)$$

Thus, for obtaining exact solution in pure bending, the numerical integration used to integrate the weak form must meet Eq. (3.26), i.e.,

$$\sum_{K=1}^{N_{\text{int}}} \mathbf{B}_I^b(\mathbf{x}_K) w_K = \mathbf{0} \quad \text{for nodes } \{I \mid \text{supp}(\Psi_I) \cap \Gamma = \emptyset\}, \quad (3.27)$$

$$\sum_{K=1}^{N_{\text{int}}} \mathbf{B}_J^b(\mathbf{x}_K) w_K = \sum_{L=1}^{N_{\text{bint}}} \mathbf{E}_J(\bar{\mathbf{x}}_L) \bar{w}_L \quad \text{for nodes } \{J \mid \text{supp}(\Psi_J) \cap \Gamma^h \neq \emptyset\}, \quad (3.28)$$

where  $N_{\text{int}}$  and  $N_{\text{bint}}$  are the total number of integration points for domain and boundary integrations, respectively,  $\mathbf{x}_K$  is the domain integration point,  $\bar{\mathbf{x}}_L$  is the boundary integration point, and  $w_K$  and  $\bar{w}_L$  are the corresponding integration weights for domain and boundary integrations, respectively.

## 4. Stabilized conforming nodal integration in Mindlin–Reissner plate

### 4.1. Curvature smoothing

The integration constraints identified in Eqs. (3.27) and (3.28) are the criteria for meshfree method to fulfill BE in the Galerkin approximation of Mindlin–Reissner plate. An SCNI is proposed here (1) to stabilize numerical instability in the nodally integrated weak form, and (2) to satisfy bending integration constraints and thus fulfill BE. This is achieved by introducing the following curvature smoothing at nodal point  $\mathbf{x}_K$ :

$$\tilde{\kappa}_{\alpha\beta}(\mathbf{x}_K) = \frac{1}{A_k} \int_{\Omega_K} \kappa_{\alpha\beta}(\mathbf{x}) \, d\Omega = \frac{1}{2A_K} \int_{\Omega_K} (\theta_{\alpha,\beta} + \theta_{\beta,\alpha}) \, d\Omega, \tag{4.1}$$

where  $A_K$  is the nodal representative area that can be obtained from, for example, Voronoi diagram shown in Fig. 2. To meet integration constraints for nodal integration, we further employ the divergence theorem in Eq. (4.1) to yield

$$\tilde{\kappa}_{\alpha\beta}(\mathbf{x}_K) = \frac{1}{2A_K} \int_{\Gamma_K} (\theta_\alpha n_\beta + \theta_\beta n_\alpha) \, d\Gamma, \tag{4.2}$$

where  $\Gamma_K$  is the boundary of representative domain  $\Omega_K$  and  $\mathbf{n}$  is the outward normal of boundary  $\Gamma_K$  as shown in Fig. 2. Introducing MLS/RK approximation of  $\theta_\alpha$  in Eq. (3.1) into Eq. (4.2) gives

$$\tilde{\mathbf{k}}^h(\mathbf{x}_K) = \sum_{I=1}^{NP} \tilde{\mathbf{B}}_I^b(\mathbf{x}_K) \mathbf{d}_I, \tag{4.3}$$

$$\tilde{\mathbf{B}}_I^b(\mathbf{x}_K) = \begin{pmatrix} 0 & \tilde{\nabla}_1 \Psi_I(\mathbf{x}_K) & 0 \\ 0 & 0 & \tilde{\nabla}_2 \Psi_I(\mathbf{x}_K) \\ 0 & \tilde{\nabla}_2 \Psi_I(\mathbf{x}_K) & \tilde{\nabla}_1 \Psi_I(\mathbf{x}_K) \end{pmatrix}, \tag{4.4}$$

$$\tilde{\nabla}_\alpha \Psi_I(\mathbf{x}_K) = \frac{1}{A_K} \int_{\Gamma_K} \Psi_I(\mathbf{x}) n_\alpha(\mathbf{x}) \, d\Gamma. \tag{4.5}$$

Following the derivation in [6], it can be shown that  $\sum_{K=1}^{NP} \tilde{\nabla}_\alpha \Psi_I(\mathbf{x}_K) A_K = 0$  for  $\{I | \text{supp}(\Psi_I) \cap \Gamma = \emptyset\}$ , and  $\sum_{K=1}^{NP} \tilde{\nabla}_\alpha \Psi_I(\mathbf{x}_K) A_K = \sum_{K=1}^{NP} \int_{\Gamma_K} \Psi_I(\mathbf{x}) n_\alpha(\mathbf{x}) \, d\Gamma = \int_{\Gamma^h} \Psi_I n_\alpha \, d\Gamma$  for  $\{J | \text{supp}(\Psi_J) \cap \Gamma^h \neq \emptyset\}$ . This follows immediately that the integration constraints in Eqs. (3.27) and (3.28) are satisfied as long as the same numerical boundary integration is used for  $\int_{\Gamma_K} \Psi_I(\mathbf{x}) n_\alpha(\mathbf{x}) \, d\Gamma$  in Eq. (4.5) and in the external force vector associated with the applied bending moment in Eq. (3.23).

#### 4.2. Discretization of weak form

The smoothed curvature and the MLS/RK approximation are incorporated into the nodally integrated weak form of Mindlin–Reissner plate by an assumed strain method [23] as follows:

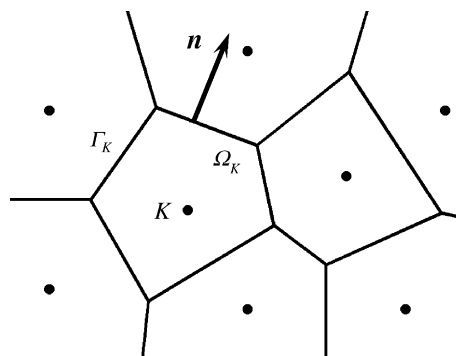


Fig. 2. Two-dimensional nodal representative domain.

$$\sum_{K=1}^{NP} (\delta \tilde{\boldsymbol{\kappa}}^{hT}(\mathbf{x}_K) \mathbf{D}^b \tilde{\boldsymbol{\kappa}}^h(\mathbf{x}_K) + \delta \boldsymbol{\gamma}^{hT}(\mathbf{x}_K) \mathbf{D}^s \boldsymbol{\gamma}^h(\mathbf{x}_K)) A_K = \sum_{I=1}^{NP} \delta w^h(\mathbf{x}_K) q(\mathbf{x}_K) A_K - \sum_{K=1}^{Nb_{int}} (\delta \boldsymbol{\theta}^{hT}(\bar{\mathbf{x}}_K) \bar{\mathbf{m}}(\bar{\mathbf{x}}_K)) \bar{w}_K, \tag{4.6}$$

where  $\mathbf{x}_K$  is nodal point coordinate,  $A_K$  is the nodal representative area used in the curvature smoothing of Eq. (4.1),  $\bar{\mathbf{x}}_K$  and  $\bar{w}_K$  are the integration points and weight for boundary integral that are consistent with the boundary integral of smoothed strain in Eq. (4.5),  $Nb_{int}$  is the number of boundary integration points, and  $\tilde{\boldsymbol{\kappa}}^h(\mathbf{x}_K)$  and  $\boldsymbol{\gamma}^h(\mathbf{x}_K)$  are approximated by

$$\tilde{\boldsymbol{\kappa}}^h(\mathbf{x}_K) = \sum_{I=1}^{NP} \tilde{\mathbf{B}}_I^b(\mathbf{x}_K) \mathbf{d}_I, \tag{4.7}$$

$$\boldsymbol{\gamma}^h(\mathbf{x}_K) = \sum_{I=1}^{NP} \mathbf{B}_I^s(\mathbf{x}_K) \mathbf{d}_I, \tag{4.8}$$

where  $\tilde{\mathbf{B}}_I^b(\mathbf{x}_K)$  and  $\mathbf{B}_I^s$  are given in Eqs. (4.4) and (3.5), respectively. The resulting discrete equation reads

$$\mathbf{K} \mathbf{d} = \mathbf{f}, \tag{4.9}$$

$$\mathbf{K} = \mathbf{K}^b + \mathbf{K}^s, \tag{4.10}$$

where

$$\mathbf{K}_{IJ}^b = \sum_{K=1}^{NP} \tilde{\mathbf{B}}_I^{bT}(\mathbf{x}_K) \mathbf{D}^b \tilde{\mathbf{B}}_J^b(\mathbf{x}_K) A_K, \tag{4.11}$$

$$\mathbf{K}_{IJ}^s = \sum_{K=1}^{NP} \mathbf{B}_I^{sT}(\mathbf{x}_K) \mathbf{D}^s \mathbf{B}_J^s(\mathbf{x}_K) A_K, \tag{4.12}$$

$$\mathbf{f}_I = \sum_{K=1}^{Nb_{int}} \Psi_I(\bar{\mathbf{x}}_K) \begin{pmatrix} 0 \\ -\bar{m}_1(\bar{\mathbf{x}}_K) \\ -\bar{m}_2(\bar{\mathbf{x}}_K) \end{pmatrix} \bar{w}_K + \sum_{K=1}^{NP} \Psi_I(\mathbf{x}_K) \begin{pmatrix} q(\mathbf{x}_K) \\ 0 \\ 0 \end{pmatrix} A_K. \tag{4.13}$$

## 5. Numerical examples

### 5.1. Timoshenko beam

Since Timoshenko beam is a one-dimensional degeneration of Mindlin–Reissner plate, this problem is first analyzed to examine the effectiveness of proposed method in lower dimension. Shape functions with quadratic basis functions that meet KMRC are employed. In this study, direct nodal integration (DNI), Gauss integration (GI) with 5-point quadrature rule, and SCNI (SCNI) are employed to integrate the discrete equilibrium equation for comparison. A normalized support size (support size divided by the averaged nodal distance) is 2.5 through out this study.

#### 5.1.1. Pure bending

The geometry and material properties of a Timoshenko beam subjected to a tip unit moment as shown in Fig. 3 are given as: length  $L = 10$ , thickness  $t = 0.1$ , Young’s modulus  $E = 2 \times 10^6$ . The analytical solution for this problem is

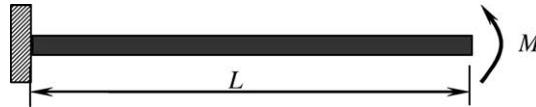


Fig. 3. Beam under pure bending.

$$w(x) = Mx^2/2EI, \tag{5.1}$$

$$\theta(x) = Mx/EI. \tag{5.2}$$

A non-uniform point distribution shown as solid circles in Fig. 4 is used to discretize the beam. The errors of numerical solutions are normalized with respect to the analytical solution. The numerical results for pure bending in Fig. 4 show an unstable solution in DNI. The GI with 5-point quadrature rule also generates noticeable error. On the other hand, the proposed SCNI leads to an exact solution regardless of non-uniform discretization.

5.1.2. Clamped–clamped beam subjected to center point load

A clamped–clamped beam is subjected to a point load  $P = 1$  at the middle point as shown in Fig. 5. The geometry and material properties are: length  $L = 10$ , Young’s modulus  $E = 2 \times 10^6$ . Due to the symmetry only half span is modeled. The analytical solution of beam deflection is

$$w(x) = \frac{P}{EI} (x^3/12 - Lx^2/16). \tag{5.3}$$

The L2 error norms of  $w$  solved using DNI, GI and SCNI for length to thickness ratio of 1000 are shown in Fig. 6. The results demonstrate the superior convergence behavior of SCNI compared to GI and DNI. Fig. 7 presents a locking test using a 6-node discretization for half beam, and the numerical solution of mid-point deflection is normalized by the analytical solution. The results show a significant locking in GI, whereas the proposed SCNI provides a locking-free solution. The transverse displacement and moment distributions for a non-uniform discretization are plotted in Figs. 8 and 9, respectively (solid circles denote the nodal locations). The numerical results show that SCNI solution is stable and most accurate compared with DNI and GI.

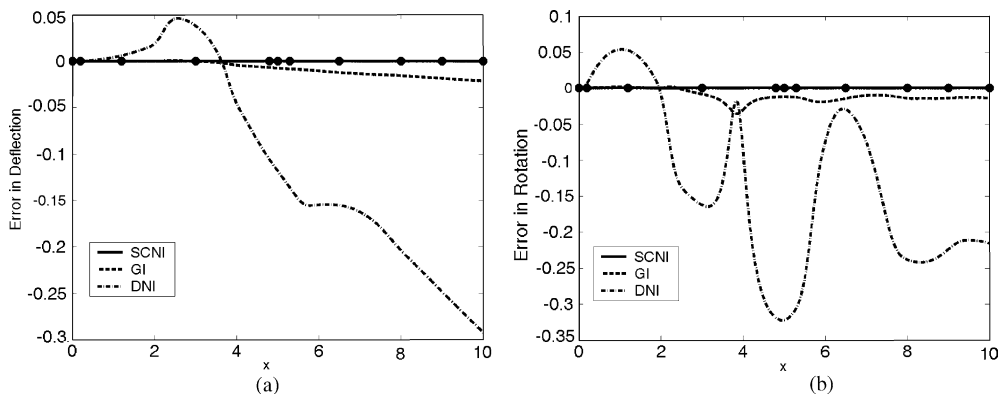


Fig. 4. Solution errors in beam subjected to a pure bending: (a) tip deflection of beam subjected to a pure bending; (b) tip rotation.

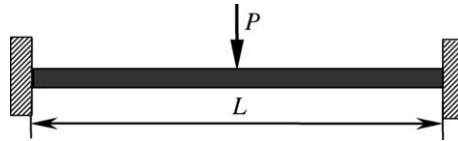


Fig. 5. Clamped-clamped beam subjected to a center point load.

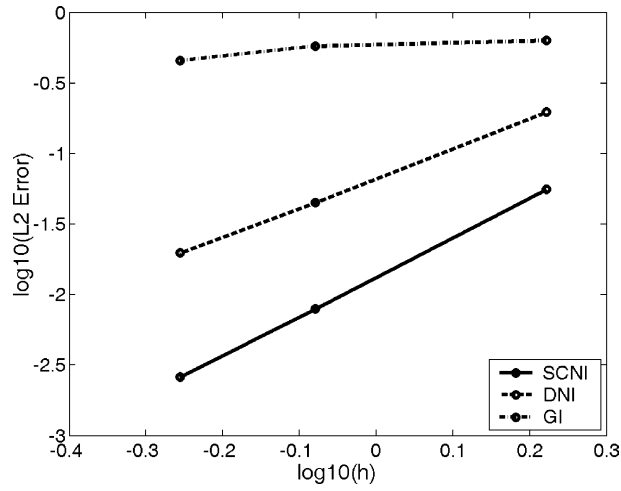


Fig. 6. L2 error norm of deflection in clamped-clamped beam problem.

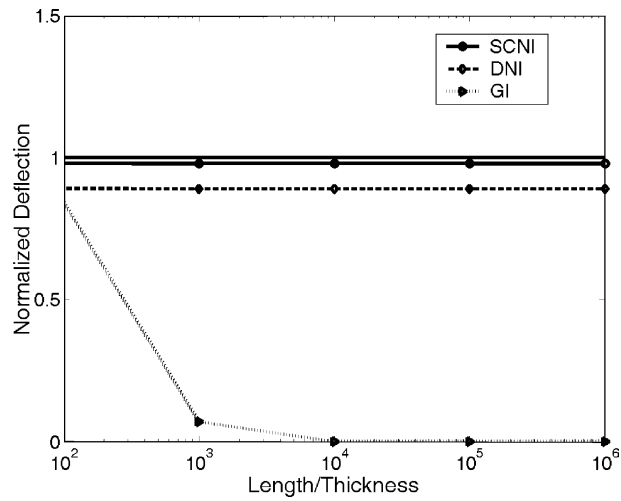


Fig. 7. Locking test in the clamped-clamped beam problem.

5.2. Mindlin–Reissner plate

In the following examples, Mindlin–Reissner plate problems are analyzed using shape functions with quadratic bases that meet KMRC, and cubic B-spline function is employed as the kernel function. Solu-

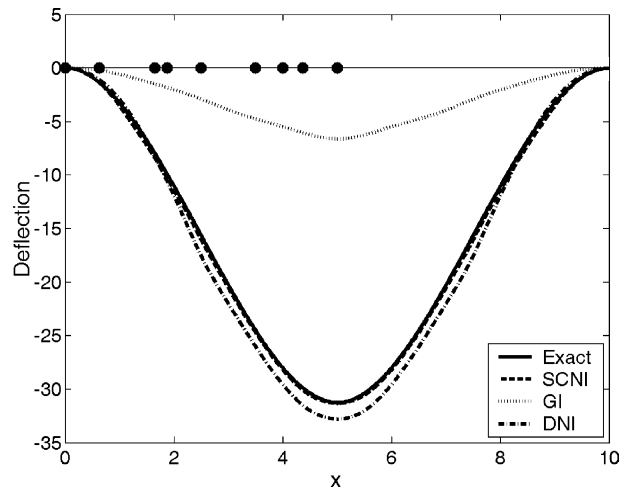


Fig. 8. Clamped-clamped beam solved by non-uniform discretization.

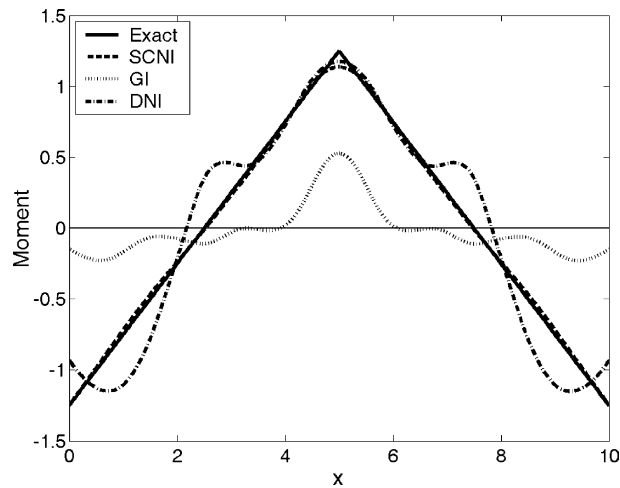


Fig. 9. Moment distribution of irregular discretization in clamped-clamped beam.

tions are obtained using DNI, GI with  $5 \times 5$  quadrature rule, and SCNI for the integration of weak form. A normalized support size of 2.5 is used through out this study.

5.2.1. *Pure bending in plate*

A pure bending problem is analyzed to verify bending exactness using different integration methods. Consider a square plate with dimension  $L = 10$ , thickness  $t = 0.1$ , Young’s modulus  $E = 2 \times 10^6$ , and Poisson’s ratio  $\nu = 0.3$ . The following pure bending deformation is imposed on the boundaries of the plate:

$$w = \frac{x^2 + xy + y^2}{1000}, \tag{5.4}$$

$$\theta_x = \frac{\partial w}{\partial x} = \frac{2x + y}{1000}, \quad (5.5)$$

$$\theta_y = \frac{\partial w}{\partial y} = \frac{x + 2y}{1000}. \quad (5.6)$$

The discretization of the plate is shown in Fig. 10. The solutions obtained using SCNI are exact in  $w$ ,  $\theta_x$ ,  $\theta_y$  up to machine precision. On the other hand, the solution of DNI presents noticeable errors in the order of 10% at some points, and the error of GI solution is of the order of 1%.

### 5.2.2. Circular plate subjected to point load

A circular clamped plate subjected to a concentrated load  $P$  at the plate centroid is analyzed Figs. 11 and 12. The material and geometry parameters are Young's modulus  $E = 3 \times 10^6$ , Poisson's ratio  $\nu = 0.3$ , plate radius  $R = 10$ , thickness  $t = 0.2$ . The analytical deflection is given by

$$w(r) = \frac{PR^2}{16\pi D} \left[ 1 - \left(\frac{r}{R}\right)^2 + 2\left(\frac{r}{R}\right)^2 \ln \frac{r}{R} \right], \quad (5.7)$$

$$D = \frac{Et^3}{12(1 - \nu^2)}, \quad (5.8)$$

where  $r$  is the distance measured from the plate center. Note that the analytical solution of a Mindlin–Reissner plate exhibits a singularity at the point load location, and thus the numerical solutions are normalized with the analytical solution evaluated at  $r = 10^{-4}R$ . In Fig. 13, the solution of meshfree method using SCNI is compared favorably with the solutions of a heterosis element (QHS) [12,13] and a serendipity finite element using reduced integration (QSR) [22]. The L2 error norms of meshfree solutions of a plate with thickness of 0.02 using DNI, GI and SCNI are also shown in Fig. 14, and superior performance of SCNI over DNI and GI is observed.

### 5.2.3. Clamped square plate subjected to a point load

A clamped square plate subjected to a center unit point load is analyzed as shown in Fig. 15. The geometry and material parameters are: Young's modulus  $E = 3 \times 10^6$ , Poisson's ratio  $\nu = 0.3$ , dimension

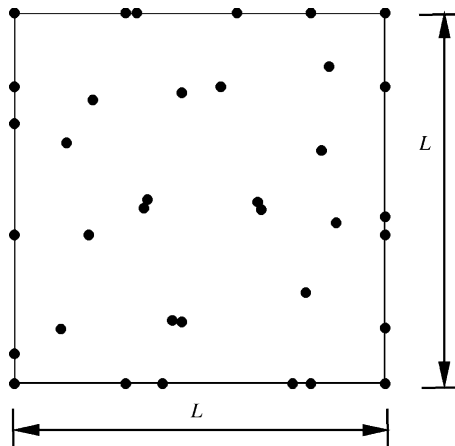


Fig. 10. Non-uniform discretization of plate under pure bending.

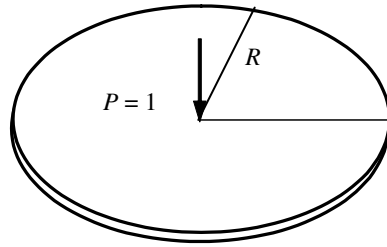


Fig. 11. Clamped circular plate subjected to a center point load.

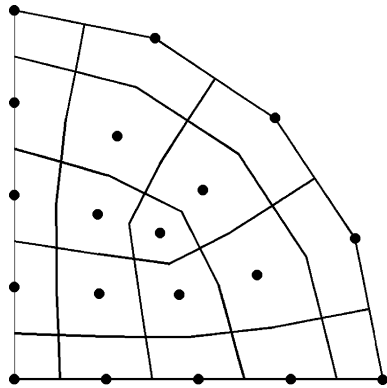


Fig. 12. Discretization of a quarter circular plate.

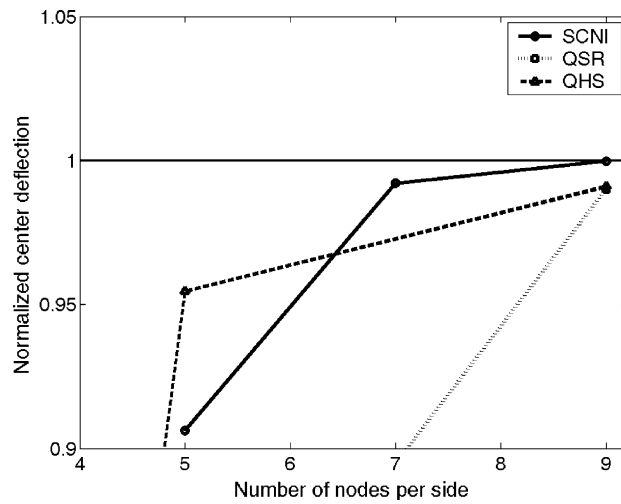


Fig. 13. Convergence comparison in a circulate plate problem.

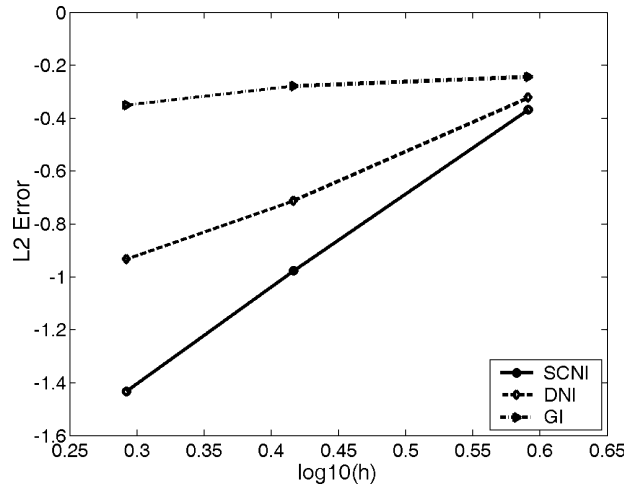


Fig. 14. L2 error comparison in a circulate plate problem.

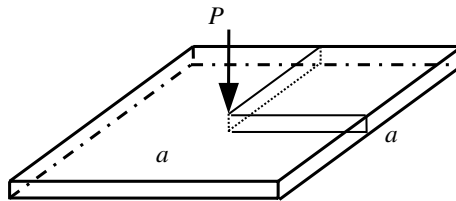


Fig. 15. Clamped plate subjected to a center point load.

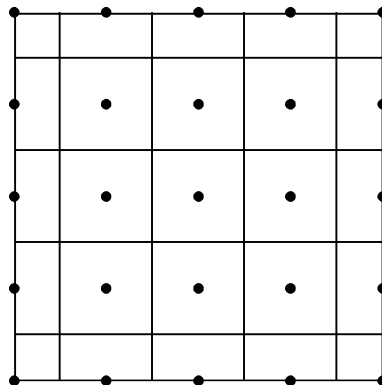


Fig. 16. A discretization of quarter plate with 25 nodes.

$a = b = 80$ , thickness  $t = 0.8$ . The analytical solution for this problem can be found in [24], where the deflection at the plate centroid is

$$w_o = c \frac{Pa^2}{D}. \tag{5.9}$$

The coefficient  $c$  is a function of the dimension ratio  $a/b$  (see [24]) and  $D$  is the flexural rigidity of plate in Eq. (5.8).

Due to symmetry, only one quarter of the plate is modeled. A 25-node discretization is shown in Fig. 16. Note that the analytical solution of a Mindlin–Reissner plate exhibits a singularity at the point load location, and thus the numerical solutions are normalized with the analytical solution evaluated at a distance  $d = 10^{-4}a$ . The SCNI meshfree solution is compared favorably with the solutions of Non-conforming Quadratic Heterosis element (NC-QH) [17], the serendipity finite element using reduced integration (QSR) [22], and the heterosis element (QHS) [12,13] in Fig. 17. The locking-free performance of the proposed SCNI method is also shown in the locking test in Fig. 18, where GI solution exhibits a severe locking.

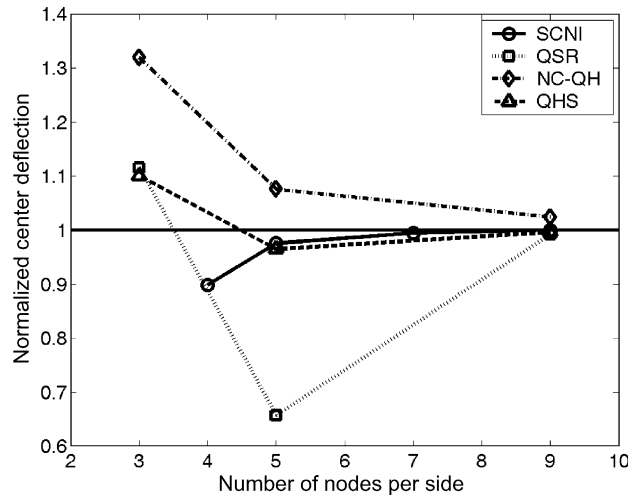


Fig. 17. Convergence comparison in a clamped square plate problem.

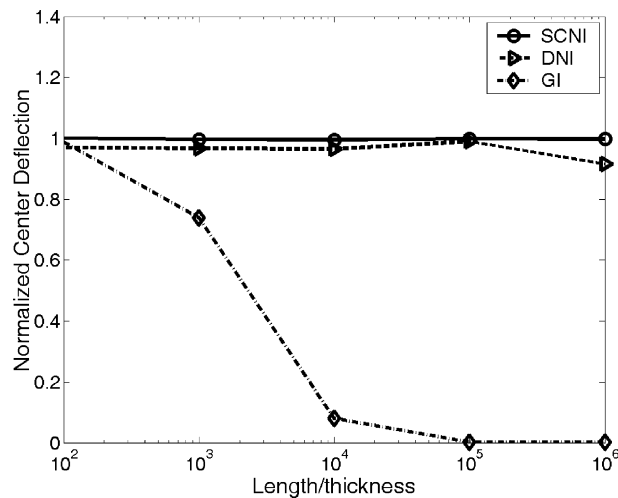


Fig. 18. Locking test in a clamped square plate problem.

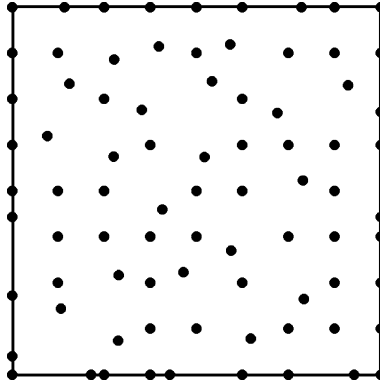


Fig. 19. Discretization of a quarter of a clamped square plate.

The numerical performance using a non-uniform discretization as shown in Fig. 19 is also studied for the case thickness  $t = 0.08$ . The normalized center deflection solution obtained by SCNI is 99.9%, compared to the accuracy of 90% from DNI, and a severe locking of 16% accuracy using GI. This study shows that the shear locking difficulty in the meshfree solution of Mindlin–Reissner plate theory in the limit of thin plate can be corrected by SCNI for both uniform and non-uniform discretizations.

## 6. Conclusion

The ability to represent pure bending mode without producing parasitic shear mode is critical to the performance of numerical method for solving shear deformable Mindlin–Reissner plate problems. In this paper, this requirement has been achieved by introducing Kirchhoff mode reproducing conditions (KMRC) in the construction of shape functions for the translational and rotational degrees of freedom of the plate. To further eliminate shear locking in the Mindlin–Reissner plate, the bending integration constraints for achieving bending exactness in the Galerkin approximation of Mindlin–Reissner plate have been derived. An SCNI that employs curvature smoothing stabilization in the nodally integrated weak form to meet the bending integration constraints and thus fulfill the bending exactness has been proposed.

In this paper, the numerical results obtained by the proposed SCNI method have been compared with those obtained by using direct nodal integration (DNI) and Gauss integration (GI) with  $5 \times 5$  quadrature rule. It has been shown that SCNI produces exact solutions with arbitrary node discretization in Timoshenko beam as well as Mindlin–Reissner plate subjected to pure bending. On the other hand, noticeable errors existed in the pure bending tests using GI, and significant discrepancy appeared using DNI. In the limit of thin plate, SCNI showed no sign of shear locking for both uniform and non-uniform discretizations, whereas GI method led to a severe shear locking in both cases. The SCNI method also demonstrated superior convergence rates over those of GI and DNI. Particularly, DNI results showed instabilities and poor accuracy in both shear deformable beams and plates.

## Acknowledgements

The support of this work by NSF/DARPA OPAAL Program under grant DMS 98-74015 and General Motors under the grant 17994902 to UCLA is greatly acknowledged.

## References

- [1] S. Beissel, T. Belytschko, Nodal integration of the element-free Galerkin method, *Comput. Methods Appl. Mech. Eng.* 139 (1996) 49–74.
- [2] T. Belytschko, Y.Y. Lu, L. Gu, Element-free Galerkin methods, *Int. J. Numer. Methods Eng.* 37 (1994) 229–256.
- [3] T. Belytschko, Y. Kronggauz, D. Organ, M. Fleming, P. Krysl, Meshless methods: an overview and recent developments, *Comput. Methods Appl. Mech. Eng.* 139 (1996) 3–47.
- [4] J.S. Chen, H.P. Wang, Some recent improvements in meshfree methods for incompressible finite elasticity boundary value problems with contact, *Comput. Mech.* 25 (2000) 137–156.
- [5] J.S. Chen, S. Yoon, H.P. Wang, W.K. Liu, An improved reproducing kernel particle method for nearly incompressible hyperelastic solids, *Comput. Methods Appl. Mech. Eng.* 181 (2000) 117–145.
- [6] J.S. Chen, C.T. Wu, S. Yoon, Y. You, A stabilized conforming nodal integration for Galerkin meshfree methods, *Int. J. Numer. Methods Eng.* 50 (2001) 435–466.
- [7] J.S. Chen, C.T. Wu, S. Yoon, Nonlinear version of stabilized conforming nodal integration for Galerkin meshfree methods, *Int. J. Numer. Methods Eng.* 53 (2002) 2587–2615.
- [8] J. Dolbow, T. Belytschko, Volumetric locking in the element free Galerkin method, *Int. J. Numer. Methods Eng.* 46 (1999) 925–942.
- [9] B. Donning, W.K. Liu, Meshless methods for shear-deformable beams and plates, *Comput. Methods Appl. Mech. Eng.* 152 (1998) 47–72.
- [10] O. Garcia, E.A. Fancello, C.S. Barcellos, C.A. Duarte, Hp-clouds in Mindlin's thick plate model, *Int. J. Numer. Methods Eng.* 47 (2000) 1381–1400.
- [11] A. Huerta, S. Fernández-Méndez, Locking in the incompressible limit for the element free Galerkin method, *Int. J. Numer. Methods Eng.* 51 (2001) 1361–1383.
- [12] T.J.R. Hughes, M. Cohen, The heterosis finite element for plate bending, *Comput. & Structures* 9 (1978) 445–450.
- [13] T.J.R. Hughes, *The Finite Element Method: Linear Static and Dynamic Finite Element Analysis*, Dover publications, Mineola, NY, 2000.
- [14] W. Kanok-Nukulchai, W. Barry, K. Saran-Yasoontorn, P.H. Bouillard, On elimination of shear locking in the element-free Galerkin method, *Int. J. Numer. Methods Eng.* 52 (2001) 705–725.
- [15] P. Krysl, T. Belytschko, Analysis of thin plates by the element-free Galerkin method, *Comput. Mech.* 16 (1995) 1–10.
- [16] P. Krysl, T. Belytschko, Analysis of thin shells by the element-free Galerkin method, *Int. J. Numer. Methods Eng.* 33 (1996) 3057–3080.
- [17] S.H. Kim, C.K. Choi, Improvement of quadratic finite element for Mindlin plate bending, *Int. J. Numer. Methods Eng.* 34 (1992) 197–208.
- [18] P. Lancaster, K. Salkauskas, Surfaces generated by moving least squares methods, *Math. Comput.* 37 (1981) 141–158.
- [19] W.K. Liu, S. Jun, Y.F. Zhang, Reproducing kernel particle methods, *Int. J. Numer. Methods Fluids* 20 (1995) 1081–1106.
- [20] W.K. Liu, S. Jun, S. Li, J. Adee, T. Belytschko, Reproducing kernel particle methods for structural dynamics, *Int. J. Numer. Methods Eng.* 38 (1995) 1655–1679.
- [21] W.K. Liu, S. Li, T. Belytschko, Moving least square kernel Galerkin method, Part I: methodology and convergence, *Comput. Methods Appl. Mech. Eng.* 143 (1997) 422–433.
- [22] E.D.L. Pugh, E. Hinton, O.C. Zienkiewicz, A study of quadrilateral plate bending elements with reduced integration, *Int. J. Numer. Methods Eng.* 12 (1978) 1059–1079.
- [23] J.C. Simo, T.J.R. Hughes, On the variational foundation of assumed strain method, *J. Appl. Mech.* 53 (1986) 51–54.
- [24] S.P. Timoshenko, S. Woinowsky-Krieger, *Theory of Plates and Shells*, second ed., McGraw-Hill, New York, 1959.